




Article

# Electrical Properties and Chemical Resistance of the Composites $(1-x)\text{Gd}_2\text{Zr}_2\text{O}_7 \cdot x\text{MgO}$ in Li-Containing Chloride Melts

Irina Anokhina <sup>1</sup>, Irina Animitsa <sup>1,\*</sup>, Maxim Erzhenkov <sup>1</sup>, Vladimir Voronin <sup>1,2</sup>, Nadezhda Kadyrova <sup>3</sup> and Yuri Zaikov <sup>1</sup>

<sup>1</sup> Institute of High Temperature Electrochemistry of the Ural Branch of the Russian Academy of Sciences, 620990 Yekaterinburg, Russia

<sup>2</sup> Institute of Metal Physics of the Ural Branch of the Russian Academy of Sciences, 620108 Yekaterinburg, Russia

<sup>3</sup> Institute of Solid State Chemistry of the Ural Branch of the Russian Academy of Sciences, 620990 Yekaterinburg, Russia

\* Correspondence: irina.animitsa@urfu.ru

**Abstract:** Composites of  $(1-x)\text{Gd}_2\text{Zr}_2\text{O}_7 \cdot x\text{MgO}$  were prepared by mixing gadolinium zirconate with freshly precipitated  $\text{Mg}(\text{OH})_2$  followed by heat treatment at 1500 °C. Small concentrations of magnesium oxide dissolved in the complex oxide matrix of  $\text{Gd}_2\text{Zr}_2\text{O}_7$ . This led to decrease in the lattice parameters of the matrix phase and a complex redistribution of Gd and Zr over the A and B sublattices. According to the impedance spectroscopy results of the studied samples, for  $(1-x)\text{Gd}_2\text{Zr}_2\text{O}_7 \cdot x\text{MgO}$  ( $x = 0.05, 0.07, 0.10$ ), the ionic conductivity was slightly higher than that for the undoped  $\text{Gd}_2\text{Zr}_2\text{O}_7$ . The share of dominant ion transport did not change upon doping with magnesium oxide. The composites showed chemical resistance in a lithium halide (LiCl) melt and interacted with  $\text{LiCl} \cdot x\text{Li}_2\text{O}$  ( $x = 2 \text{ wt.}\%, 4 \text{ wt.}\%$ ) melts at 650 °C with the formation of a  $\text{Gd}_2\text{O}_3$  phase or a mixture of phases ( $\text{Gd}_2\text{O}_3$ ,  $\text{Li}_2\text{ZrO}_3$ ,  $\text{ZrO}_2$ ,  $\text{LiGdO}_2$ , or  $\text{LiGdCl}_2$ ) on the ceramic surface, respectively.

**Keywords:** composite; pyrochlore; gadolinium zirconate;  $\text{Gd}_2\text{Zr}_2\text{O}_7$ ; oxide ion conductivity; chemical stability in Li-containing halide melts



**Citation:** Anokhina, I.; Animitsa, I.; Erzhenkov, M.; Voronin, V.; Kadyrova, N.; Zaikov, Y. Electrical Properties and Chemical Resistance of the Composites  $(1-x)\text{Gd}_2\text{Zr}_2\text{O}_7 \cdot x\text{MgO}$  in Li-Containing Chloride Melts. *Processes* **2023**, *11*, 1217. <https://doi.org/10.3390/pr11041217>

Academic Editor: Gang Wang

Received: 28 February 2023

Revised: 23 March 2023

Accepted: 3 April 2023

Published: 14 April 2023



**Copyright:** © 2023 by the authors. Licensee MDPI, Basel, Switzerland. This article is an open access article distributed under the terms and conditions of the Creative Commons Attribution (CC BY) license (<https://creativecommons.org/licenses/by/4.0/>).

## 1. Introduction

The pyrochemical processing of spent nuclear fuel is an effective way to reduce nuclear waste. Processes such as anodic dissolution, mass transfer, and the electrodeposition of actinides in molten salts have been studied in detail by scientists around the world [1–4]. The electrochemical reduction of SNF to a metallic form is the main stage of the electrorefining process for  $\text{LiCl} \cdot x\text{Li}_2\text{O}$  melts. As a result, actinide metal oxides are deposited on the cathode, while due to the proximity of electrode potentials, metallic lithium is formed on the cathode, which participates in the process of chemical reduction of actinide oxides. To obtain a high-quality product and avoid undesirable processes, such as the dissolution of the platinum anode at a low content of  $\text{Li}_2\text{O}$  in the melt, i.e., ~0.25–0.50 wt.%, the lack of solubility of plutonium and americium oxides at high contents of  $\text{Li}_2\text{O}$ , at ~3.4 wt.% and ~5.1 wt.%, respectively, or the degradation of structural materials, it is necessary to maintain a certain concentration of oxide ions in the working melt [5]. Therefore, devices for the continuous monitoring of the oxygen ion content in the working  $\text{LiCl} \cdot x\text{Li}_2\text{O}$  melt environment are needed.

Most of the ion-selective membrane sensors proposed for fabrication are made of ceramic materials, which must be inert in  $\text{LiCl}$ -based melts containing  $\text{Li}_2\text{O}$ . Materials based on zirconium oxide used in oxide-halide melts are not stable enough to maintain stable operation for a long time. The formation of  $\text{Li}_2\text{ZrO}_3$  is inevitable when using  $\text{ZrO}_2$  in  $\text{LiCl} \cdot x\text{Li}_2\text{O}$  melts, and with an increase in the content of  $\text{Li}_2\text{O}$ , the stoichiometry of lithium zirconate changes to  $\text{Li}_6\text{Zr}_2\text{O}_7$  and  $\text{Li}_8\text{ZrO}_6$  [6–8]. The coating of ceramics with a layer

of lithium zirconate changes the conductivity from oxygen ion to cationic transport (by  $\text{Li}^+$ -ions) [9–14]. The instability of electrolytes based on  $\text{ZrO}_2$  in the corrosive environment of  $\text{Li}^+$ -containing melts [15–17] has stimulated the search for alternative materials—that is, sensors of the activity of  $\text{O}^{2-}$  ions in melts.

One of the promising materials with high oxygen ionic conductivity is the  $\text{Gd}_2\text{Zr}_2\text{O}_7$  solid electrolyte with a pyrochlore structure. It is known that the structure of gadolinium zirconate withstands high doses of radiation due to the ability of the structure to endure cationic disorder. Under the action of radiation, the structure can undergo a structural phase transition from pyrochlore to a structure of defective fluorite, without being subjected to amorphization. In this regard,  $\text{Gd}_2\text{Zr}_2\text{O}_7$  is considered as a matrix for radioactive waste disposal [18–22]. Gadolinium zirconate is also used as a material for thermal barrier coatings [20–22], catalysts [23,24], solid electrolytes for SOFCs [25,26], and sensors [27].

The sensory activity of gadolinium zirconate has been insufficiently studied. However, there is evidence showing that when testing  $\text{Ca}^{+2}$ -doped  $\text{Gd}_2\text{Zr}_2\text{O}_7$  as a  $\text{NO}_2$  sensor at 500 °C, the device showed the highest current value and the fastest response time, as well as the fastest recovery time. The results obtained were better than those of the commercial YSZ-based sensor [28].

In order to explore the possibility of using the material in the chloride melt as a sensor, it is necessary to study its chemical stability in the melt. For this purpose, it is necessary to determine the range of dopants that can ensure the acquisition of a high-density ceramic material with high, dominant oxygen ion conductivity. Previously, it was found that the use of lithium as a dopant for the  $\text{Gd}_2\text{Zr}_2\text{O}_7$  phase makes it possible to increase the oxygen ion conductivity but does not make it possible to obtain high-density ceramics [29,30]. Therefore, the problem of searching for dopants for the  $\text{Gd}_2\text{Zr}_2\text{O}_7$  phase remains relevant.

It has been established [31] that the homogeneous magnesium doping of  $\text{Gd}_2\text{Zr}_2\text{O}_7$  (solid-solution  $\text{Gd}_{2-x}\text{Mg}_x\text{Zr}_2\text{O}_{7-x/2}$ ) can prevent the ion exchange of high-density ceramics with  $\text{LiCl-xLi}_2\text{O}$  melts up to a  $\text{Li}_2\text{O}$  concentration of 4 wt.%. Thus, a small concentration of magnesium is assumed to be able to protect the material from interaction with the melt [32]. For this article, materials based on  $\text{Gd}_2\text{Zr}_2\text{O}_7$  were chosen as the objects of study. In order to obtain high-density  $\text{Gd}_2\text{Zr}_2\text{O}_7$  ceramics, a composite with  $\text{MgO}$  additive was used. Composites based on gadolinium zirconate  $(1-x)\text{Gd}_2\text{Zr}_2\text{O}_7 \cdot x\text{MgO}$  were investigated for their chemical resistance in oxide-chloride lithium melts for the first time. The structure and transport properties of  $(1-x)\text{Gd}_2\text{Zr}_2\text{O}_7 \cdot x\text{MgO}$  were also studied for the first time.

## 2. Materials and Methods

Composites of  $(1-x)\text{Gd}_2\text{Zr}_2\text{O}_7 \cdot x\text{MgO}$  were prepared by mixing gadolinium zirconate  $\text{Gd}_2\text{Zr}_2\text{O}_7$  with magnesium hydroxide. Gadolinium zirconate was synthesized by mixing with the starting reagents  $\text{Gd}_2\text{O}_3$  (99.998%, VEKTON, RF) and  $\text{ZrO}_2$  (99.99%, REACHIM, RF). The oxide powders were ground together in a planetary ball mill (Fritsch Planetary Micro Mill Pulverisette 7, Fritsch GmbH, Federal Republic of Germany) with a rotation speed of 350 rpm in ethanol-exploiting zirconium balls for 8 h. After milling, the mixture was dried and annealed at 1200–1400 °C with steps of 100 °C. Freshly precipitated  $\text{Mg}(\text{OH})_2$  was obtained from  $\text{MgCO}_3$  (99.99%, VEKTON, RF). The  $\text{MgCO}_3$  was dissolved in dilute nitric acid with a pH ~2–3, and then the resulting  $\text{Mg}(\text{NO}_3)_2$  was caused to interact with a solution of  $\text{NH}_4\text{OH}$  with the formation of a corresponding precipitate. The obtained  $\text{Mg}(\text{OH})_2$  was dried and mixed with  $\text{Gd}_2\text{Zr}_2\text{O}_7$  in the amount required for the preparation of the samples of  $(1-x)\text{Gd}_2\text{Zr}_2\text{O}_7 \cdot x\text{MgO}$  ( $x = 0.05, 0.07, 0.10$ ). The corresponding calculations were carried out taking into account TG studies of the obtained  $\text{Mg}(\text{OH})_2$ . The resulting mixture was ground in the planetary ball mill at a rotation speed of 700 rpm for 2 h in ethanol. Then, the dried mixtures were pressed into cylindrical briquettes and treated at a temperature of 1500 °C for 12 h. The sintering of the cylindrical briquettes of undoped  $\text{Gd}_2\text{Zr}_2\text{O}_7$  was carried out at a temperature of 1550 °C for 15 h.

A crystal structure analysis of the samples was conducted using an X-ray diffractometer with  $\text{Cu-K}\alpha$  radiation (scanning rate of 0.5 °/min, steps of 0.01°) (Rigaku MiniFlex600,

Japan) and the SmartLab Studio II (Rigaku, Japan) software with the PDF-2 2019 database (ICDD, USA). Silicon powder (NIST640f) was used as the external standard. The FullProf program was used for the refinement of the parameters with the Rietveld method.

Scanning electron microscopy of the sintered samples was conducted with Phenom ProX (Phenom-World, Holland). Before analysis, the surfaces of the samples were polishing on a diamond wheel. The composition of the samples was determined using energy-dispersive X-ray spectroscopy with a silicon drift detector and Phenom Pro Suite software.

The average density of the ceramics was determined using the geometric method. The value of the crystallographic density of the samples was taken as the standard.

The measurements of *ac* electrical conductivity, as a function of temperature and oxygen partial pressure, were made using the impedance spectroscopy method (Elins Z-1000P spectrometer, Elins Ltd., Moscow, Russia) in air over a temperature range of 300–1000 °C with cooling of 1 °/min and a  $pO_2$  range of  $1 \times 10^{-18}$ –0.21 atm. The surfaces of the cylindrical-shaped samples were covered with platinum paste. The electrodes were burned in air at a temperature of 900 °C for 3 h. The ZView-4.0 software (Scribner Associate Inc., Southern Pines, NC, USA) was used to treat the impedance data. The oxygen partial pressure measurements were performed using an 8 mol.%  $Y_2O_3$ -stabilized zirconia (YSZ) sensor and an oxygen pump.

The stability of the ceramic composite samples was assessed in a glove box (SPEKS GB, Russia) in an argon atmosphere with an impurity oxygen content less than 2 ppm and a water content less than 1 ppm. The salts LiCl, LiCl-2 wt.%  $Li_2O$ , and LiCl-4 wt.%  $Li_2O$  were placed in a glassy carbon crucible. The salts LiCl (CAS No: 7447-41-8, Leverton Clarke Ltd., Basingstoke, UK) and  $Li_2O$  (99.5 wt.%, Alfa Aesar, Haverhill, MA, USA) were used for the experiment. Before the experiment, the LiCl salt was subjected to additional purification by zone recrystallization. The salt in the crucible was heated in a shaft furnace at a temperature of 650 °C. The temperature in the working area was controlled using a Pt-Pt(Rh) thermocouple. The ceramics were preliminarily weighed on a balance and dried in an oven at 200 °C. They were then immersed in a melt of the corresponding salt. Exposure in the salt melts was carried out for 48 h. After holding in the melt, the samples were removed and washed in distilled water and ethanol. After drying the samples in an oven at 200 °C, the composites were analyzed by XRD and SEM.

The components of the melt were analyzed before the experiment and after 8, 16, 24, and 48 h by chemical analysis with inductively coupled plasma atomic emission spectroscopy (Optima 4300 DV Perkin Elmer spectrometer, USA).

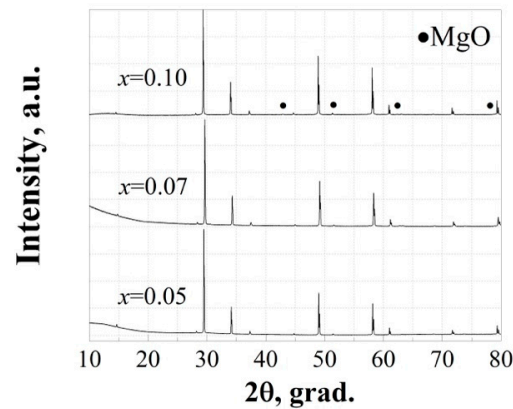
### 3. Results

#### 3.1. X-ray Analysis and SEM Characterization

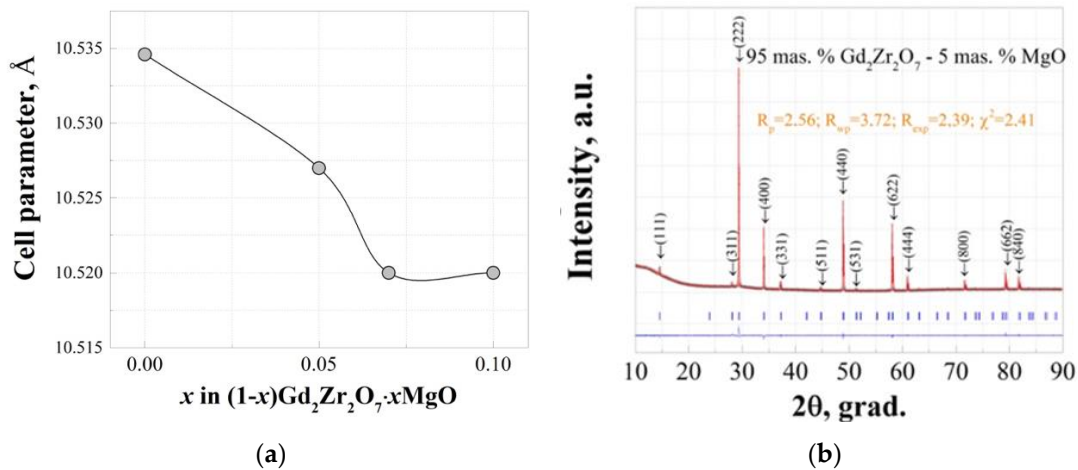
The interpretation of the X-ray spectra (Figure 1) showed that the main phase in all the obtained composites was  $Gd_2Zr_2O_7$  with a pyrochlore structure (space group Fd-3m). The  $0.90Gd_2Zr_2O_7-0.10MgO$  composite contained a small amount of the second phase, which corresponded to the magnesium oxide. According to the XRD data, the samples with additives of MgO at the amounts of 5 wt.% and 7 wt.% were single-phase.

The lattice parameter decreased with the addition of MgO up to 7 wt.% (Figure 2a). However, the parameter remained unchanged over the concentration range of 7–10 wt.%.

The change in the lattice parameter indicates the formation of solid solution due to the dissolution of magnesium in the structure and the redistribution of cations between the A and B sublattices. The redistribution of cations with different ionic radii will affect the lattice parameter [33]. Figure 2b shows the X-ray pattern of the  $0.95Gd_2Zr_2O_7-0.05MgO$  sample processed using the Rietveld method in the FullProf program. In Figure 2b, one can see the diffraction data, which were treated using a gadolinium and zirconium redistributed model (Table 1). However, the inversion degree between the A and B sublattices grew from 8.15% ( $0.95Gd_2Zr_2O_7-0.05MgO$ ) to 12.7% ( $0.90Gd_2Zr_2O_7-0.10MgO$ ) with the increase in the Mg content.



**Figure 1.** X-ray patterns obtained in air after annealing of the composites at 1500 °C: (1-x)Gd<sub>2</sub>Zr<sub>2</sub>O<sub>7</sub>·xMgO. The black dots denote the MgO phase reflections.



**Figure 2.** (a) Graph of the dependence of the lattice parameter on the composition. (b) X-ray diffraction pattern of the 0.95Gd<sub>2</sub>Zr<sub>2</sub>O<sub>7</sub>–0.05MgO sample processed using the FullProf program.

**Table 1.** The refined coordinates of atoms of 0.95Gd<sub>2</sub>Zr<sub>2</sub>O<sub>7</sub>–0.05MgO in a cubic unit cell (space group Fd-3m) in the Gd and Zr disorder model.

Atom	Wyckhoff Symbol	x/a	y/b	z/c	Occupancy
Gd	16c	0.000	0.000	0.000	1.837 (5)
Zr	16c	0.000	0.000	0.000	0.163 (5)
Zr	16d	0.500	0.500	0.500	1.837 (5)
Gd	16d	0.500	0.500	0.500	0.163 (5)
O1	48f	0.411	0.125	0.125	6.00 (5)
O2	8a	0.125	0.125	0.125	1.00 (0)

$$R_p = 2.56, R_{wp} = 3.72, R_{exp} = 2.39, R_b = 3.67, R_f = 4.59, \chi^2 = 2.41.$$

The size of the Mg<sup>2+</sup> ion is smaller than the Gd<sup>3+</sup> ion in eightfold coordination [33]; thus, the parameter may decrease. In this regard, we assume that part of the Mg<sup>2+</sup> dopes the Gd<sub>2</sub>Zr<sub>2</sub>O<sub>7</sub> matrix and occupies the Gd<sup>3+</sup> position (Table 2). Noting the misunderstanding of the exact amount of magnesium oxide included in this calculation, we considered the limited case, where the minimum concentration of the composite additive was included in the Gd<sub>2</sub>Zr<sub>2</sub>O<sub>7</sub> structure. Accordingly, we can write the composition 0.95Gd<sub>2</sub>Zr<sub>2</sub>O<sub>7</sub>–0.05MgO as a solid solution: Gd<sub>1.88</sub>Mg<sub>0.05</sub>Zr<sub>0.07</sub>Zr<sub>1.93</sub>Gd<sub>0.07</sub>O<sub>7</sub>. The introduction of magnesium is accompanied by an increase in the degree of order of 0.95Gd<sub>2</sub>Zr<sub>2</sub>O<sub>7</sub>–0.05MgO by 11.4% compared to the undoped sample. In our previous work [31], it was shown that the intro-



duction of magnesium into the structure could be achieved at an amount of 0.05 wt.%, and the calculations were conducted using the Rietveld method.

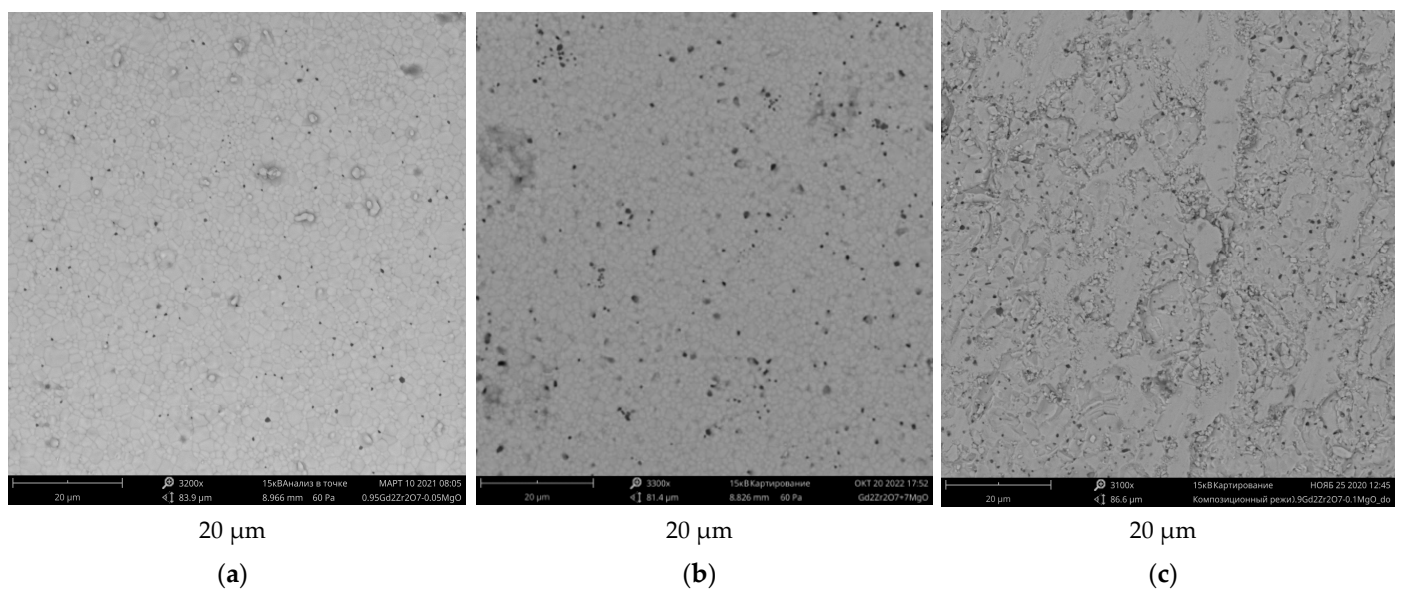
**Table 2.** The refined coordinates of atoms of  $0.95\text{Gd}_2\text{Zr}_2\text{O}_7-0.05\text{MgO}$  in a cubic unit cell (space group Fd-3m), with Gd and Mg existing in the A sublattice.

Atom	Wyckhoff Symbol	x/a	y/b	z/c	Occupancy
Gd	16c	0.000	0.000	0.000	1.880 (5)
Zr	16c	0.000	0.000	0.000	0.070 (5)
Mg	16c	0.000	0.000	0.000	0.050
Zr	16d	0.500	0.500	0.500	1.930 (5)
Gd	16d	0.500	0.500	0.500	0.070 (5)
O1	48f	0.412	0.125	0.125	5.56 (2)
O2	8a	0.125	0.125	0.125	1.00 (0)
O3	8b	0.375	0.375	0.375	0.44 (2)

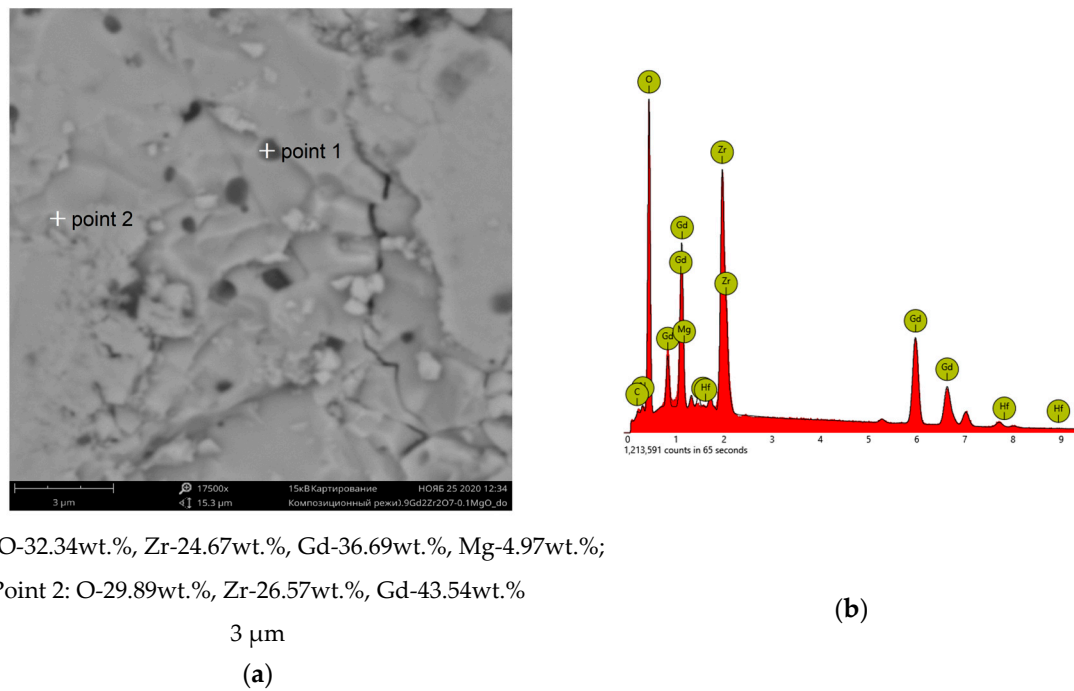
$R_p = 2.46$ ,  $R_{wp} = 3.54$ ,  $R_b = 3.61$ ,  $R_f = 4.19$ ,  $\chi^2 = 3.23$ .

The calculations performed for the two different models of  $0.95\text{Gd}_2\text{Zr}_2\text{O}_7-0.05\text{MgO}$  sample presented in Tables 1 and 2 show close results regarding the obtained calculation errors. It is probable that the lattice parameter is affected by a complex process associated with the disordering of the cationic and anionic sublattices, as well as the presence of small amounts of magnesium. Thus, to describe the structure of the obtained composites, one must not be limited to the X-ray method alone.

The SEM images confirm that all the  $(1-x)\text{Gd}_2\text{Zr}_2\text{O}_7 \cdot x\text{MgO}$  samples contain impurities of MgO. Figure 3a–c shows densely sintered grains in the main phase, which tend to coalesce with each other with an increase in the concentration of MgO additive. Additionally, in all the SEM figures, there are dark spots of poorly crystallized (amorphous) phase. The EDS spectra show that such poorly crystallized spots belong to phase with an increased magnesium content (Figure 4a,b), and we believe that this is magnesium oxide. It is probable that due to amorphization, the low concentration of the composite additive MgO ( $x = 0.05$  and  $x = 0.07$ ) does not enable its identification in the composites by X-ray diffraction.



**Figure 3.** SEM images of  $(1-x)\text{Gd}_2\text{Zr}_2\text{O}_7 \cdot x\text{MgO}$  samples at (a)  $x = 0.05$ ; (b)  $x = 0.07$ ; (c)  $x = 0.10$ .



**Figure 4.** (a) SEM images of  $0.90\text{Gd}_2\text{Zr}_2\text{O}_7-0.10\text{MgO}$ . (b) EDS spectra of  $0.90\text{Gd}_2\text{Zr}_2\text{O}_7-0.10\text{MgO}$  in point 3.

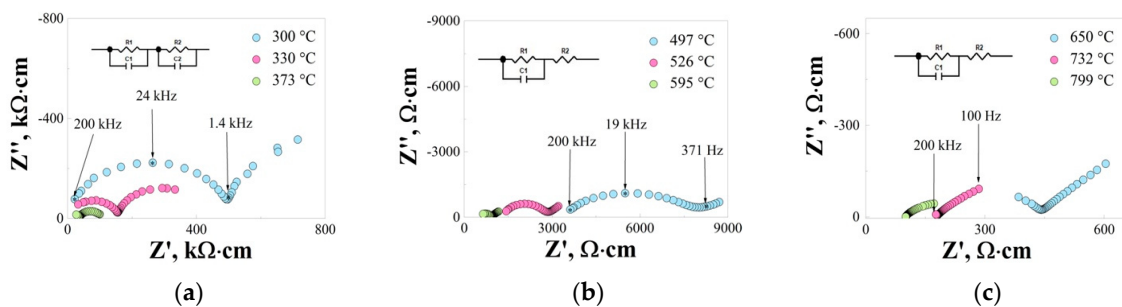
The relative densities of the obtained samples are all close to each other (Table 3), and there is a slight tendency for the relative density to increase with the content of magnesium oxide. It should be emphasized that higher temperatures and holding times are required to obtain high-density ceramics of undoped  $\text{Gd}_2\text{Zr}_2\text{O}_7$ . Therefore, it can be concluded that the MgO additive contributes to an increase in the sinterability of the material, as shown in previous works [34,35].

**Table 3.** The relative density of  $\text{Gd}_2\text{Zr}_2\text{O}_7$  and  $(1-x)\text{Gd}_2\text{Zr}_2\text{O}_7 \cdot x\text{MgO}$  samples.

Chemical Formula	$\rho$ , %
$\text{Gd}_2\text{Zr}_2\text{O}_7$	96d24
$0.95\text{Gd}_2\text{Zr}_2\text{O}_7-0.05\text{MgO}$	96.40
$0.93\text{Gd}_2\text{Zr}_2\text{O}_7-0.07\text{MgO}$	96.83
$0.90\text{Gd}_2\text{Zr}_2\text{O}_7-0.10\text{MgO}$	97.27

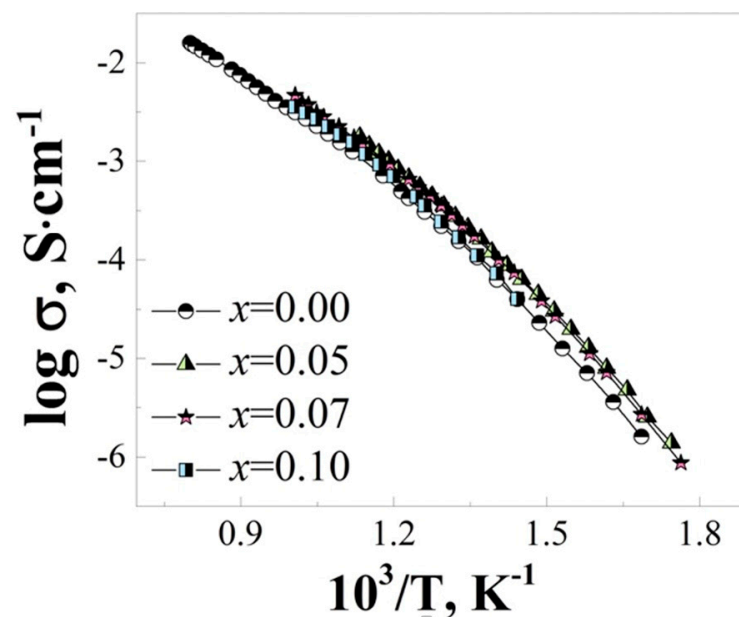
### 3.2. Electrical Conductivities

Well-resolved impedance hodographs, obtained in the range from  $300\text{ }^\circ\text{C}$  to  $1000\text{ }^\circ\text{C}$  in air, are presented as two semicircles (Figure 5).



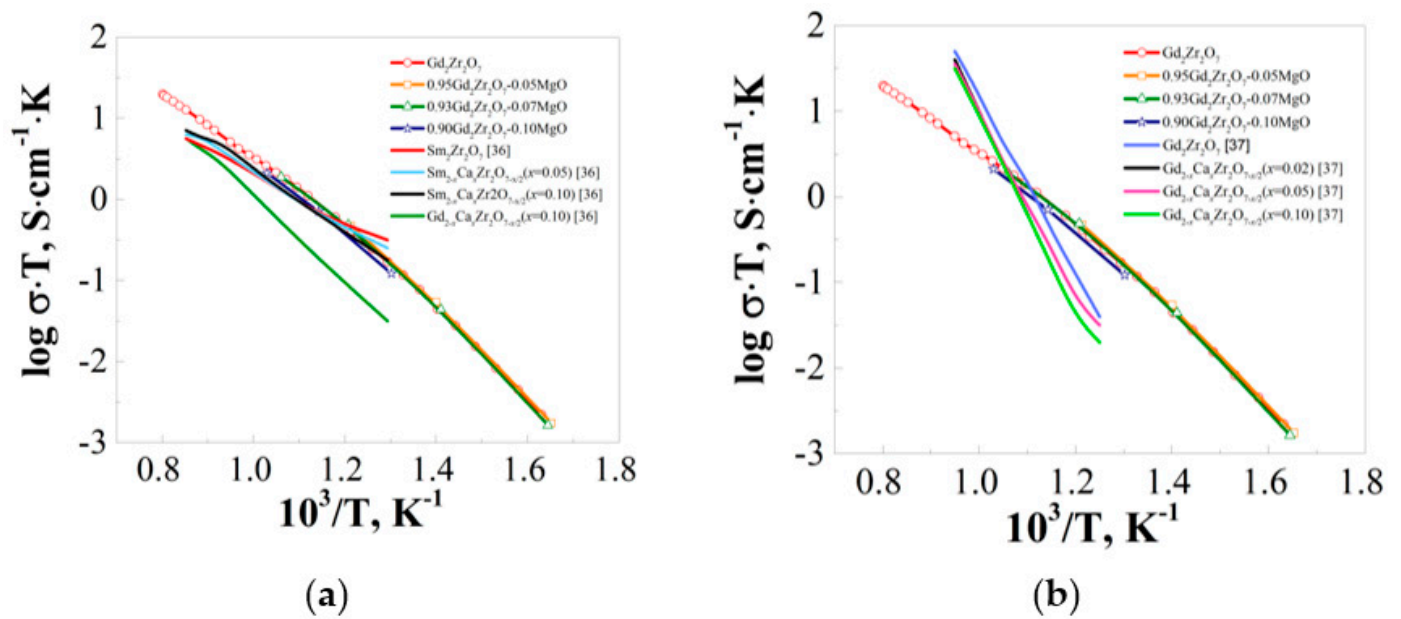
**Figure 5.** Impedance hodographs of  $0.95\text{Gd}_2\text{Zr}_2\text{O}_7-0.05\text{MgO}$  obtained in air in the temperature ranges of (a)  $300-373\text{ }^\circ\text{C}$ , (b)  $497-595\text{ }^\circ\text{C}$ , and (c)  $650-799\text{ }^\circ\text{C}$ .

It was possible to separate the volume and grain boundary contributions to the total electrical conductivity. One semicircle, with a capacity of  $C = 10^{-11} \text{ F}\cdot\text{cm}^{-1}$ , exceeds zero and is responsible for the bulk properties of the sample, and the second one, with a capacity of  $C = 10^{-9} \text{ F}\cdot\text{cm}^{-1}$ , is responsible for the properties of the grain boundaries. By extrapolating the first semicircle to the OX axis, the bulk electrical conductivity was determined. The value of the bulk electrical conductivity of  $(1-x)\text{Gd}_2\text{Zr}_2\text{O}_7\cdot x\text{MgO}$ , shown in Figure 6, is slightly increased compared to that of the undoped  $\text{Gd}_2\text{Zr}_2\text{O}_7$  with a pyrochlore structure over the entire temperature range. The electrical conductivities of all the doped samples are close to each other. This effect is probably due to acceptor doping and the formation of oxygen vacancies.



**Figure 6.** Temperature dependence of bulk electrical conductivity for the  $(1-x)\text{Gd}_2\text{Zr}_2\text{O}_7\cdot x\text{MgO}$  composites.

The results obtained here were compared with the literature data on the conductivity of the most highly conductive phases [36,37]. Figure 7 shows the bulk conductivities of the materials with a pyrochlore structure. The electrical conductivity of the highly conductive phase  $\text{Sm}_{2-x}\text{Ca}_x\text{Zr}_2\text{O}_{7-x/2}$  ( $x = 0, 0.05, 0.10$ ) [36] is comparable with the data that we obtained for the composite  $(1-x)\text{Gd}_2\text{Zr}_2\text{O}_7\cdot x\text{MgO}$ . It can also be concluded (Figure 7a) that these samples have similar activation energies. Calcium doping of the gadolinium sublattice in  $\text{Gd}_2\text{Zr}_2\text{O}_7$  ( $\text{Gd}_{2-x}\text{Ca}_x\text{Zr}_2\text{O}_{7-x/2}$  ( $x = 0.10$ )) significantly reduced the conductivity of the material. It can be seen in [37] that all the obtained samples have different activation energies of  $\text{Gd}_{2-x}\text{Ca}_x\text{Zr}_2\text{O}_{7-x/2}$ , and the electrical conductivity of the obtained compositions sharply decreases in the region of medium temperatures (Figure 7b). Thus, the addition of magnesium oxide  $\text{MgO}$  to gadolinium zirconate  $\text{Gd}_2\text{Zr}_2\text{O}_7$  did not lead to a decrease in conductivity; the values of ionic conductivity are comparable to those of the most highly conductive pyrochlores. At the same time, the addition of magnesium oxide made it possible to sinter the material at a lower temperature and obtain high-density ceramics. We believe that this method of obtaining high-density ceramics can be extended to other promising systems with a pyrochlore structure. Thus, for pyrochlores, magnesium oxide can be used both as an acceptor dopant and as a sintering additive.

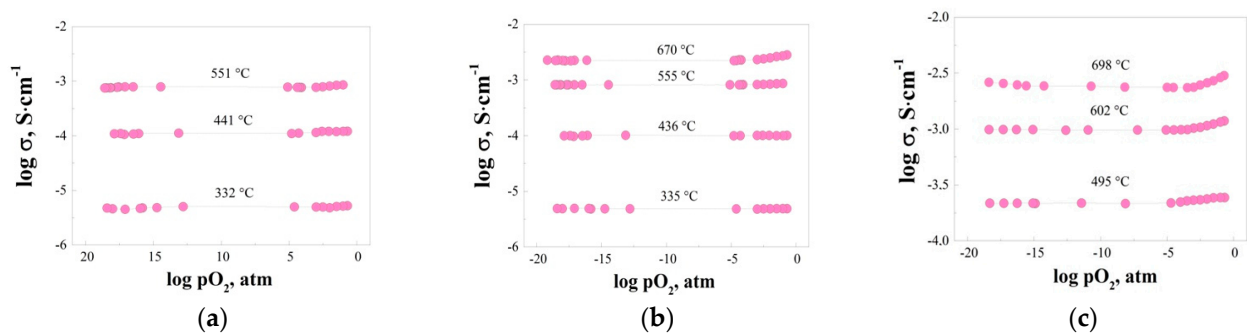


**Figure 7.** Temperature dependence of bulk electrical conductivity for the  $(1-x)\text{Gd}_2\text{Zr}_2\text{O}_7 \cdot x\text{MgO}$  composites,  $\text{Sm}_{2-x}\text{Ca}_x\text{Zr}_2\text{O}_{7-x/2}$  ( $x = 0, 0.05, 0.10$ ) [36], and  $\text{Gd}_{2-x}\text{Ca}_x\text{Zr}_2\text{O}_{7-x/2}$  ( $x = 0.10$ ) [36]. (a) Temperature dependence of bulk electrical conductivity for the  $(1-x)\text{Gd}_2\text{Zr}_2\text{O}_7 \cdot x\text{MgO}$  composites and  $\text{Gd}_{2-x}\text{Ca}_x\text{Zr}_2\text{O}_{7-x/2}$  ( $x = 0, 0.02, 0.05, 0.10$ ) [37] (b).

The transport properties of the ceramics were studied in atmospheres with different oxygen partial pressures. The differentiation of the total conductivities into their ionic ( $\sigma_{ion}$ ) and electronic ( $\sigma_{el}$ ) contributions was carried out through the analysis of the isotherms  $\log \sigma - \log p\text{O}_2$ . The total electrical conductivity ( $\sigma_{tot}$ ) obtained in air at the oxygen partial pressure ( $p\text{O}_2$ ) = 0.21 atm is the sum of the ionic and electronic conductivities (1). The ionic electrical conductivity  $\sigma_{ion}$  does not depend on  $p\text{O}_2$  (it is a plateau on the  $\log \sigma - \log p\text{O}_2$  graph).

$$\sigma_{tot} = \sigma_{el} + \sigma_{ion} \quad (1)$$

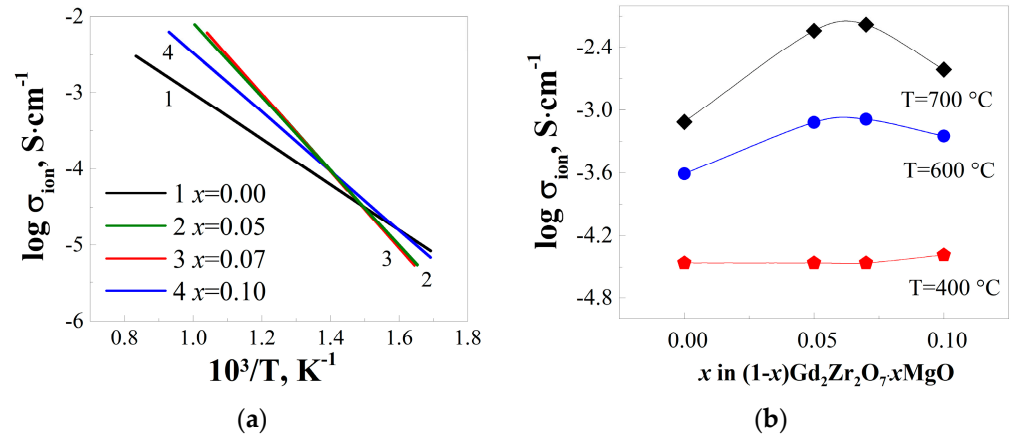
Small additions of a dopant do not change the general nature of the dependence. The isotherms of conductivity are shown in Figure 8a–c, where the plateau of ionic conductivity can be observed over the entire temperature range. With an increase in the concentration of the heterogeneous additive to  $x = 0.10$ , the plots of electrical conductivity against  $p\text{O}_2$  show a positive slope in the region of high oxygen partial pressures, which indicates the appearance of a small  $p$ -type contribution to the total conductivity of the sample.



**Figure 8.** Dependence of the electrical conductivity of the composition on the oxygen partial pressure for (a)  $0.95\text{Gd}_2\text{Zr}_2\text{O}_7-0.05\text{MgO}$ , (b)  $0.93\text{Gd}_2\text{Zr}_2\text{O}_7-0.07\text{MgO}$ , (c)  $0.90\text{Gd}_2\text{Zr}_2\text{O}_7-0.10\text{MgO}$ .

Based on the data obtained, the temperature dependence of ionic conductivity can be plotted. As can be seen in Figure 9, the ionic conductivity of all the composites is higher

than that for the undoped phase. It can be assumed that this is due to an increase in oxygen vacancies as a result of acceptor doping and a complex redistribution of cations over the A and B sublattices.



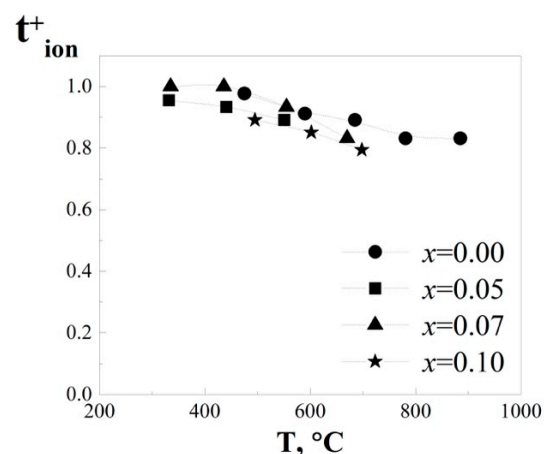
**Figure 9.** Temperature dependence of ionic conductivity (a). Dependence of ionic conductivity on x in  $(1-x)Gd_2Zr_2O_7 \cdot xMgO$  at 600 °C (b).

The ionic transport number can be calculated as:

$$t_{ion} = \frac{\sigma_{ion}}{\sigma_{tot}} \quad (2)$$

where  $\sigma_{ion}$  is the ionic conductivity from the plateau of the  $\log \sigma - pO_2$  dependencies between  $10^{-18}$  atm and  $10^{-4}$  atm, and  $\sigma_{tot}$  is the total conductivity at  $pO_2 = 0.21$  atm. As we can see from the equation, the ionic conductivity and the total conductivity increase, respectively, while the share ( $t_{ion}$ ) does not change.

The ion transport numbers of the  $(1-x)Gd_2Zr_2O_7 \cdot xMgO$  and undoped  $Gd_2Zr_2O_7$  samples are close (Figure 10). The transport numbers tend to increase with decreasing temperature and are close to unity over the entire temperature range. Thus, the addition of magnesium oxide did not affect the dominant ionic nature of transport of the  $Gd_2Zr_2O_7$  phase.



**Figure 10.** The values of the ion transfer numbers for  $(1-x)Gd_2Zr_2O_7 \cdot xMgO$  ( $x = 0, 0.05, 0.07, 0.10$ ).

### 3.3. Chemical Resistance of LiCl and LiCl-Li<sub>2</sub>O Melts

Table 4 shows photographs of the  $(1-x)Gd_2Zr_2O_7 \cdot xMgO$  ceramic samples before and after interaction with LiCl- $xLi_2O$  melts, where  $x = 0$  wt%, 2 wt%, and 4 wt% at a temperature of 650 °C. As can be seen in the photo, with an increase in the concentration of lithium oxide in the melt, the degree of destruction of the samples increases. In particular, the



0.90Gd<sub>2</sub>Zr<sub>2</sub>O<sub>7</sub>-0.10MgO sample in a LiCl melt did not undergo destruction. The same sample in the LiCl-2 wt.% Li<sub>2</sub>O melt was partially destroyed and split into three parts, and in the LiCl-4 wt.% Li<sub>2</sub>O melt, it was completely destroyed and divided into three large parts and many small parts, which also underwent dissolution, judging by the presence of a white coating on the surface of the electrolyte during the experiment and chemical analysis. High-density ceramic samples of Gd<sub>2</sub>Zr<sub>2</sub>O<sub>7</sub> were examined in our earlier work [27]; however, it was shown that Gd<sub>2</sub>Zr<sub>2</sub>O<sub>7</sub> interacted with the LiCl-2 wt.% Li<sub>2</sub>O melt during high-temperature exposure.

**Table 4.** Photographs of the obtained ceramic samples of (1-x)Gd<sub>2</sub>Zr<sub>2</sub>O<sub>7</sub>·xMgO before and after exposure in LiCl-xLi<sub>2</sub>O melts at T = 650 °C.

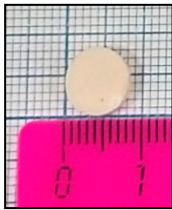
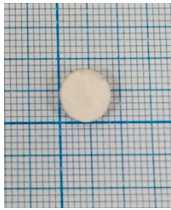
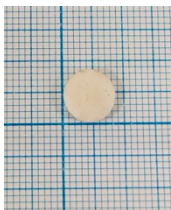
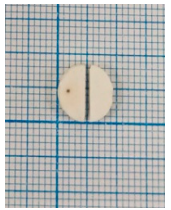
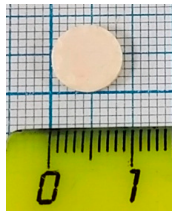

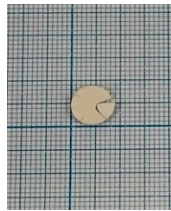

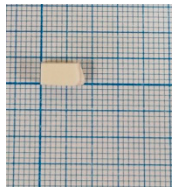
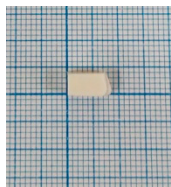
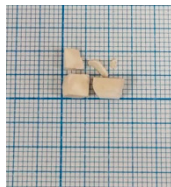
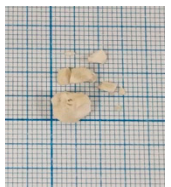
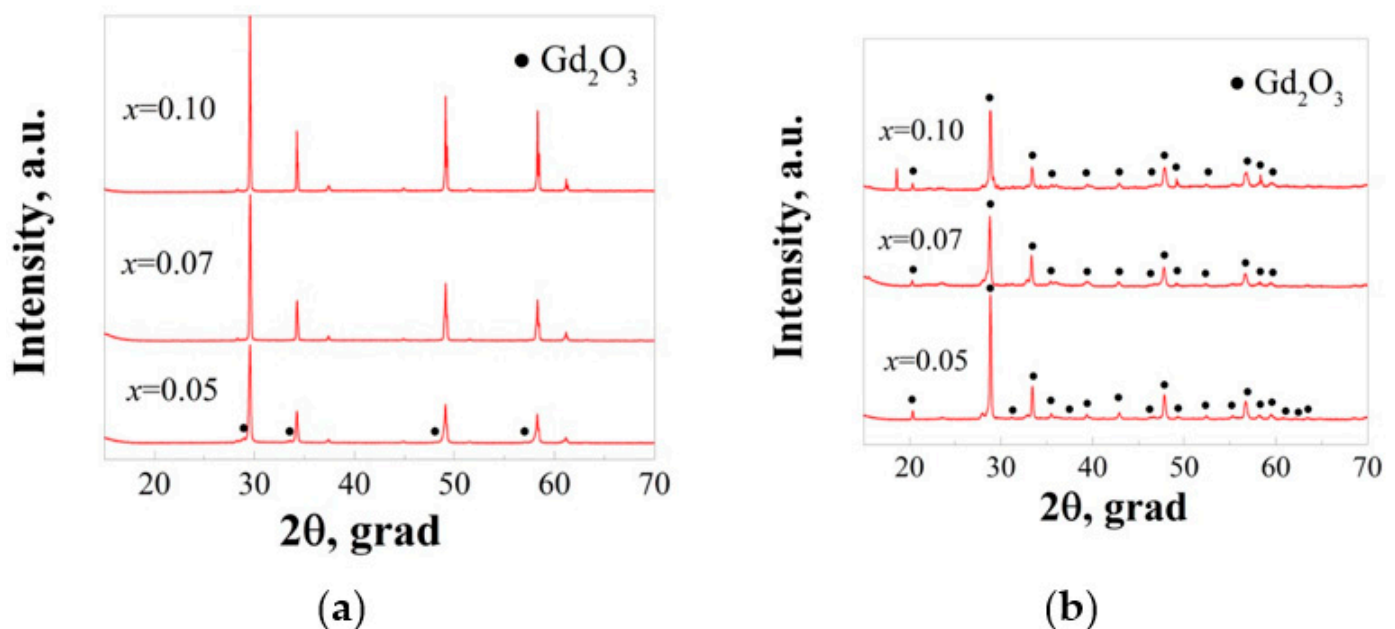
x in (1-x)Gd <sub>2</sub> Zr <sub>2</sub> O <sub>7</sub> ·xMgO	Photo before the Experiment	Photo after 48 h of Exposure in LiCl	Photo after 48 h of Exposure in LiCl-2 wt.% Li <sub>2</sub> O	Photo after 48 h of Exposure in LiCl-4 wt.% Li <sub>2</sub> O
0.05				
0.07				
0.10				

Table 5 shows the change in mass of the ceramics after the exposure of the ceramic samples of (1-x)Gd<sub>2</sub>Zr<sub>2</sub>O<sub>7</sub>·xMgO in LiCl-xLi<sub>2</sub>O melts at a temperature of 650 °C. After holding the samples in the LiCl melt, there was no significant change in the density of the ceramics and no mass loss. Despite the fact that the 0.93Gd<sub>2</sub>Zr<sub>2</sub>O<sub>7</sub>-0.07MgO ceramics cracked, the mass loss during the study was 0.01%. It is likely that the presence of small defects in the form of cracks in 0.93Gd<sub>2</sub>Zr<sub>2</sub>O<sub>7</sub>-0.07MgO significantly affected the strength characteristics of the material and led to destruction; thus, this fact should be taken into account in further studies. When 2 wt.% Li<sub>2</sub>O was added to the melt, the 0.90Gd<sub>2</sub>Zr<sub>2</sub>O<sub>7</sub>-0.10MgO ceramics were destroyed, as a result of which the mass loss was ~3%. In the melt with 4 wt.% Li<sub>2</sub>O, there was a significant mass loss in all the ceramics under study, decreasing from ~3% to ~11.5%. The greatest loss occurred in the 0.90Gd<sub>2</sub>Zr<sub>2</sub>O<sub>7</sub>-0.10MgO sample.

**Table 5.** Change in the mass loss of ceramic samples of  $(1-x)\text{Gd}_2\text{Zr}_2\text{O}_7 \cdot x\text{MgO}$  before and after exposure in  $\text{LiCl}-x\text{Li}_2\text{O}$  melts at  $T = 650^\circ\text{C}$ .

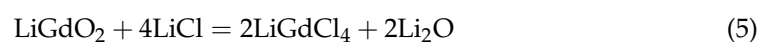
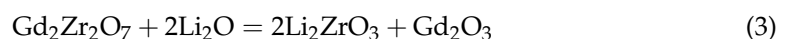
Composition	Before	After LiCl	After LiCl-2 wt.% $\text{Li}_2\text{O}$	After LiCl-4 wt.% $\text{Li}_2\text{O}$
	%	%	%	%
0.95 $\text{Gd}_2\text{Zr}_2\text{O}_7$ -0.05 $\text{MgO}$	-	+0.28	-0.07	-3.4
0.93 $\text{Gd}_2\text{Zr}_2\text{O}_7$ -0.07 $\text{MgO}$	-	-0.01	+0.09	-2.89
0.90 $\text{Gd}_2\text{Zr}_2\text{O}_7$ -0.10 $\text{MgO}$	-	-0.32	-2.73	-11.46

The X-ray phase analysis data presented in Figure 11a show that the 0.95 $\text{Gd}_2\text{Zr}_2\text{O}_7$ -0.05 $\text{MgO}$  sample interacted with the LiCl melt, since during the experiment, a phase of gadolinium oxide formed on the surface of the material. The samples (0.93 $\text{Gd}_2\text{Zr}_2\text{O}_7$ -0.07 $\text{MgO}$ , 0.90 $\text{Gd}_2\text{Zr}_2\text{O}_7$ -0.10 $\text{MgO}$ ) did not chemically interact with the working medium during the 48 h of exposure. Figure 11b shows that in a more aggressive melt containing lithium oxide at an amount of 2 wt.%, exposure led to the interaction of all the ceramics with the melt, together with the formation of a gadolinium oxide phase.

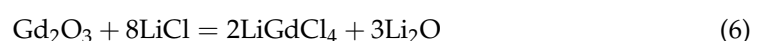


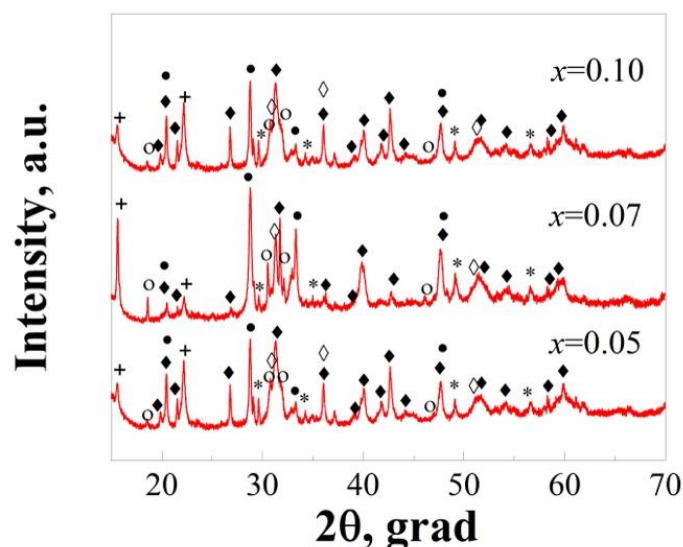
**Figure 11.** X-ray patterns of  $(1-x)\text{Gd}_2\text{Zr}_2\text{O}_7 \cdot x\text{MgO}$  after exposure at  $T = 650^\circ\text{C}$  in (a) LiCl melt and (b) LiCl-2 wt.%  $\text{Li}_2\text{O}$  melt.

The concentration of lithium oxide also significantly affects the rate of destruction of the material and the formation of end products through the chemical interaction of the material with the melt. Figure 12 shows the X-ray diffraction patterns of the composite surface after 48 h of interaction with the LiCl-4 wt.%  $\text{Li}_2\text{O}$  melt. The surface consists of a mixture of phases formed by the chemical interaction of gadolinium zirconate with the melt components. Such a process can be described by Equations (3)–(6):



or



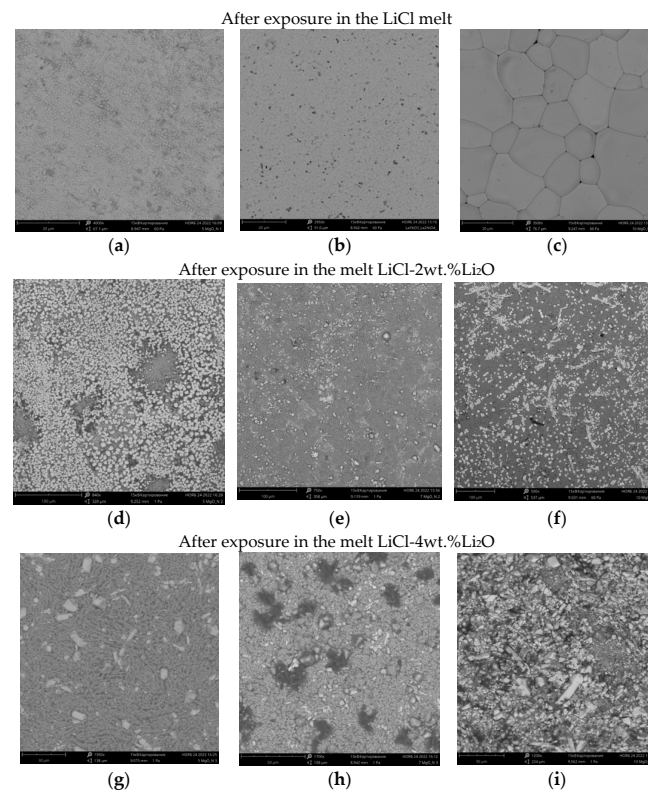


**Figure 12.** X-ray patterns of  $(1-x)\text{Gd}_2\text{Zr}_2\text{O}_7 \cdot x\text{MgO}$  ceramics after exposure in LiCl-4 wt%  $\text{Li}_2\text{O}$  melt at  $T = 650^\circ\text{C}$ . Asterisks— $\text{Gd}_2\text{Zr}_2\text{O}_7$ , black diamonds— $\text{Li}_2\text{ZrO}_3$ , black circles— $\text{Gd}_2\text{O}_3$ , white diamonds— $\text{ZrO}_2$ , white circles— $\text{LiGdO}_2$ , crosses— $\text{LiGdCl}_4$ .

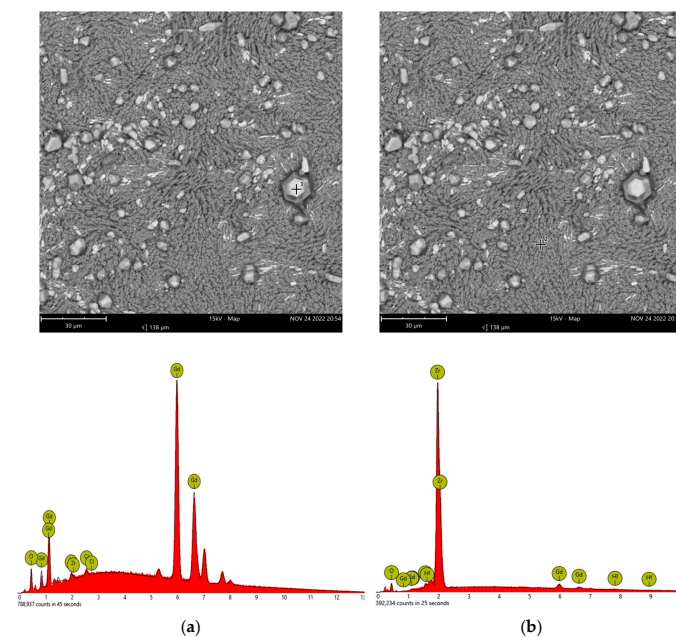
The SEM data of the composites are confirmed by the XRD data. Figure 13a–c shows the surfaces of composites exposed in a LiCl melt at a temperature of  $650^\circ\text{C}$ . It was found that the surface of  $0.95\text{Gd}_2\text{Zr}_2\text{O}_7\text{-}0.05\text{MgO}$  had grains of different contrasts. The surfaces of the remaining compositions remained identical to the initial state. The surfaces of the composites exposed in LiCl-2 wt.%  $\text{Li}_2\text{O}$  were distinguished by grains with different morphologies and contrasts which were unevenly distributed over the ceramic surfaces (Figure 13d–f). The smallest grain growth and grain concentration were recorded for the composite  $0.93\text{Gd}_2\text{Zr}_2\text{O}_7\text{-}0.07\text{MgO}$ . EDS spectra confirmed (Figure 14) that the dark surface grains corresponded to a phase with a high content of zirconium, and the light grains corresponded to a phase with a high content of gadolinium. With an increase in the content of lithium oxide to 4 wt.%, the morphology of the grains also changed (Figure 13g–i), and their enlargement occurred.

The chemical analysis of the  $(1-x)\text{Gd}_2\text{Zr}_2\text{O}_7 \cdot x\text{MgO}$  composite did not establish the presence of Gd or Zr ceramic components in the LiCl melt. With an increase in the concentration of lithium oxide in the melt, the concentrations of zirconium and gadolinium as components of the melt increased (Figure 15). Additionally, depending on the composition of the ceramics, the saturation time of the melt, with respect to gadolinium, varied. At  $x = 0.05$ , the saturation time for the LiCl-4 wt.%  $\text{Li}_2\text{O}$  melt was 8 h, and at  $x = 0.07$  and  $x = 0.10$ , the saturation times were 24 and 30 h, respectively.

Thus, the results obtained showed that the addition of magnesium oxide did not lead to an increase in the chemical stability of the phase  $\text{Gd}_2\text{Zr}_2\text{O}_7$  in the melts of LiCl- $\text{Li}_2\text{O}$ . We believe that this is due to the morphology of the obtained composites when the magnesium oxide phase was localized in the form of individual grains. It is probably that the situation would be more favorable with the addition of magnesium oxide, encapsulating the grains of the main phase,  $\text{Gd}_2\text{Zr}_2\text{O}_7$ , and preventing interaction with the melt. Since the system under study was demonstrated to be capable of obtaining high oxygen ion conductivities and high-density ceramics, it is of interest for further research, for example, using higher concentrations of magnesium oxide or changing the method for obtaining a composite. This will be the topic of our further research.

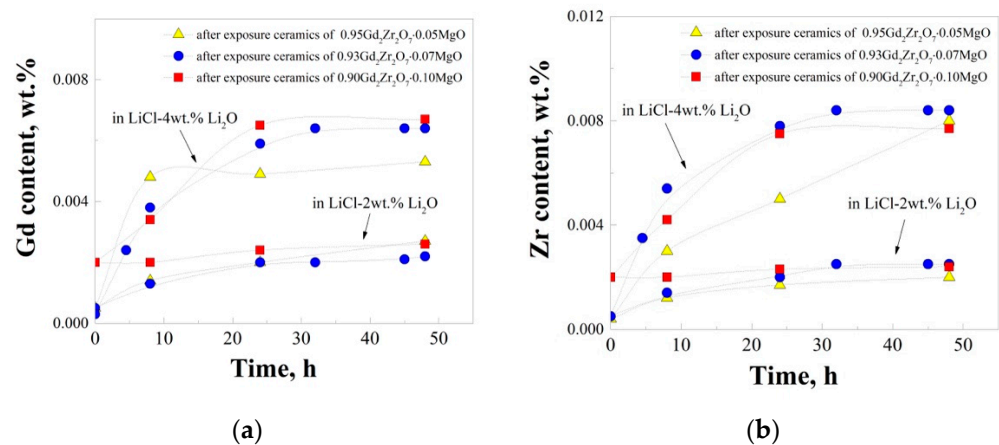


**Figure 13.** Scanning electron microscopy images of (a)  $0.95\text{Gd}_2\text{Zr}_2\text{O}_7-0.05\text{MgO}$ , (b)  $0.93\text{Gd}_2\text{Zr}_2\text{O}_7-0.07\text{MgO}$ , and (c)  $0.90\text{Gd}_2\text{Zr}_2\text{O}_7-0.10\text{MgO}$  after exposure for 48 h in LiCl at a  $T = 650\text{ }^\circ\text{C}$ . Scanning electron microscopy images of (d)  $0.95\text{Gd}_2\text{Zr}_2\text{O}_7-0.05\text{MgO}$ , (e)  $0.93\text{Gd}_2\text{Zr}_2\text{O}_7-0.07\text{MgO}$ , and (f)  $0.90\text{Gd}_2\text{Zr}_2\text{O}_7-0.10\text{MgO}$  after exposure for 48 h in a LiCl-2 wt.%  $\text{Li}_2\text{O}$  melt at  $T = 650\text{ }^\circ\text{C}$ . Scanning electron microscopy images of (g)  $0.95\text{Gd}_2\text{Zr}_2\text{O}_7-0.05\text{MgO}$ , (h)  $0.93\text{Gd}_2\text{Zr}_2\text{O}_7-0.07\text{MgO}$ , and (i)  $0.90\text{Gd}_2\text{Zr}_2\text{O}_7-0.10\text{MgO}$  after exposure for 48 h in a LiCl-4 wt.%  $\text{Li}_2\text{O}$  melt at  $T = 650\text{ }^\circ\text{C}$ .



**Figure 14.** SEM images and EDS data for the sample of  $0.90\text{Gd}_2\text{Zr}_2\text{O}_7-0.10\text{MgO}$  after exposure for 48 h in a LiCl-2 wt.%  $\text{Li}_2\text{O}$  melt at  $T = 650\text{ }^\circ\text{C}$  (a). SEM images of and EDS spectrum of the  $0.90\text{Gd}_2\text{Zr}_2\text{O}_7-0.10\text{MgO}$  sample after exposure for 48 h in the LiCl-2 wt.%  $\text{Li}_2\text{O}$  melt at  $T = 650\text{ }^\circ\text{C}$  (b).





**Figure 15.** (a) Chemical analysis data on the content of Gd in the melts after 48 h of exposure for  $(1-x)\text{Gd}_2\text{Zr}_2\text{O}_7 \cdot x\text{MgO}$ . (b) Chemical analysis data on the Zr content in the melts after 48 h of holding for  $(1-x)\text{Gd}_2\text{Zr}_2\text{O}_7 \cdot x\text{MgO}$ .

It should be emphasized that there are few studies on the chemical resistance of ceramics in halide melts. The investigations are mainly carried out for simple oxides (doped with an acceptor impurity), for example:  $\text{ZrO}_2(\text{Y}_2\text{O}_3)$ ,  $\text{ZrO}_2(\text{MgO})$ ,  $\text{ZrO}_2(\text{Sc}_2\text{O}_3)$ ,  $\text{ZrO}_2(\text{CaO})$ ,  $\text{CeO}_2(\text{Gd}_2\text{O}_3)$  [38,39]. It was shown that the increase in the content of  $\text{Li}_2\text{O}$  led to the destruction of the samples. Therefore, investigations of  $\text{Gd}_2\text{Zr}_2\text{O}_7$ -based pyrochlores are the most promising.

#### 4. Conclusions

Composites with the general formula  $(1-x)\text{Gd}_2\text{Zr}_2\text{O}_7 \cdot x\text{MgO}$  were obtained. Small concentrations of magnesium oxide were dissolved in the complex oxide matrix of  $\text{Gd}_2\text{Zr}_2\text{O}_7$  with the formation of a solid solution, which manifested itself through a decrease in the lattice parameters of the matrix phase. This led to the formation of oxygen vacancies  $V_o$  and a complex redistribution of the Gd and Zr over the A and B sublattices. The ionic conductivity of the studied samples of  $(1-x)\text{Gd}_2\text{Zr}_2\text{O}_7 \cdot x\text{MgO}$  ( $x = 0.05, 0.07, 0.10$ ) was slightly higher than that of the undoped phase. The oxygen ionic conductivity reached  $6.6 \times 10^{-3} \text{ Ohm}\cdot\text{cm}$  at  $800^\circ\text{C}$  and  $8.1 \times 10^{-4} \text{ Ohm}\cdot\text{cm}$  at  $600^\circ\text{C}$  for  $(1-x)\text{Gd}_2\text{Zr}_2\text{O}_7 \cdot x\text{MgO}$  ( $x = 0.07$ ). The transfer numbers, below  $500^\circ\text{C}$ , reached 100%. The share of dominant ion transport did not change upon doping with magnesium oxide.

Composites based on gadolinium zirconate were investigated for their chemical resistance in oxide-chloride lithium melts for the first time. Composites of  $(1-x)\text{Gd}_2\text{Zr}_2\text{O}_7 \cdot x\text{MgO}$  ( $x = 0.07, 0.10$ ) showed chemical resistance in lithium halide (LiCl) melts for 48 h at  $650^\circ\text{C}$ . However, when  $\text{Li}_2\text{O}$  was introduced into the melt at the amounts of 2 wt.% and 4 wt.%, the composites chemically interacted with the melt component ( $\text{Li}_2\text{O}$ ), with the formation of a  $\text{Gd}_2\text{O}_3$  phase or a mixture of phases ( $\text{Gd}_2\text{O}_3$ ,  $\text{Li}_2\text{ZrO}_3$ ,  $\text{ZrO}_2$ ,  $\text{LiGdO}_2$ , or  $\text{LiGdCl}_2$ ) on the ceramic surface, respectively. This interaction was also confirmed by the chemical analysis of the melt after the experiments.

Additives of magnesium oxide had a significant effect on sintering, which ensured the production of high-density samples at lower temperatures and shorter heat treatment times.

**Author Contributions:** Conceptualization, I.A. (Irina Animitsa); methodology, Y.Z. and I.A. (Irina Anokhina); X-ray diffraction analysis, V.V. and N.K.; melt research and methodology, M.E.; writing—original draft preparation, I.A. (Irina Animitsa) and I.A. (Irina Anokhina); writing—review and editing, I.A. (Irina Animitsa) and I.A. (Irina Anokhina). All authors have read and agreed to the published version of the manuscript.

**Funding:** This research received no external funding.

**Institutional Review Board Statement:** Not applicable.



**Informed Consent Statement:** Not applicable.

**Data Availability Statement:** Not applicable.

**Conflicts of Interest:** The authors declare no conflict of interest.

## References

1. Choi, E.-Y.; Hur, J.-M.; Choi, I.-K.; Kwon, S.G.; Kang, D.-S.; Hong, S.S.; Shin, H.-S.; Yoo, M.A.; Jeong, S.M. Electrochemical reduction of porous 17 kg uranium oxide pellets by selection of an optimal cathode/anode surface area ratio. *J. Nucl. Mater.* **2011**, *418*, 87–92. [[CrossRef](#)]
2. Willitt, J.L.; Miller, W.E.; Battles, J.E. Electrorefining of uranium and plutonium—A literature review. *J. Nucl. Mater.* **1992**, *195*, 229–249. [[CrossRef](#)]
3. Kurata, M.; Inoue, T.; Serp, J.; Ougier, M.; Glatz, J.-P. Electro-chemical reduction of MOX in LiCl. *J. Nucl. Mater.* **2004**, *328*, 97–102. [[CrossRef](#)]
4. Merwin, A.; Williamson, M.A.; Willitt, J.L.; Chidambaram, D. Review—Metallic Lithium and the Reduction of Actinide Oxides. *J. Electrochem. Soc.* **2017**, *164*, H5236–H5246. [[CrossRef](#)]
5. Choi, E.-Y.; Choi, I.-K.; Hur, J.-M.; Kang, D.-S.; Shin, H.-S.; Jeong, S.M. In Situ Electrochemical Measurement of  $O^{2-}$  Concentration in Molten  $Li_2O/LiCl$  during Uranium Oxide Reduction. *J. Solid State Chem.* **2012**, *15*, E11–E13. [[CrossRef](#)]
6. Sakamura, Y.; Iizuka, M.; Kitawaki, S.; Nakayoshi, A.; Kofuji, H. Formation and reduction behaviors of zirconium oxide compounds in  $LiCl-Li_2O$  melt at 923 K. *J. Nucl. Mater.* **2015**, *466*, 269–279. [[CrossRef](#)]
7. Cho, S.-H.; Kim, D.-Y.; Kwon, S.; Yoon, B.-H.; Lee, J.-H. High-temperature corrosion characteristics of yttria-stabilized zirconia material in molten salts of  $LiCl-Li_2O$  and  $LiCl-Li_2O-Li$ . *J. Nucl. Sci. Technol.* **2018**, *55*, 97–103. [[CrossRef](#)]
8. Pfeiffer, H.; Knowles, K.M. Reaction mechanisms and kinetics of the synthesis and decomposition of lithium metazirconate through solid-state reaction. *J. Eur. Ceram. Soc.* **2004**, *24*, 2433–2443. [[CrossRef](#)]
9. Pantyukhina, M.I.; Andreev, O.L.; Martem'yanova, Z.S.; Batalov, N.N. Cation Conductivity of  $Li_8ZrO_6-LiYO_2$  Solid Solutions. *Inorg. Mater.* **2004**, *40*, 404–406. [[CrossRef](#)]
10. Sherstobitova, E.A.; Gubkin, A.F.; Bobrikov, I.A.; Kalashnova, A.V.; Pantyukhina, M.I. Bottle-necked ionic transport in  $Li_2ZrO_3$ : High temperature neutron diffraction and impedance spectroscopy. *Electrochim. Acta* **2016**, *209*, 574–581. [[CrossRef](#)]
11. Hellstrom, E.E.; Gool, W.V. Li ion conduction in  $Li_2ZrO_3$ ,  $Li_4ZrO_4$ , and  $LiScO_2$ . *Solid State Ion.* **1981**, *2*, 59–64. [[CrossRef](#)]
12. Zhan, X.; Cheng, Y.-T.; Shirpour, M. Nonstoichiometry and Li-Ion Transport in Lithium Zirconate: The Role of Oxygen Vacancies. *J. Am. Ceram. Soc.* **2018**, *101*, 4053–4065. [[CrossRef](#)]
13. Pantyukhina, M.I.; Obrosof, V.P.; Stepanov, A.P.; Voronin, V.I.; Batalov, N.N. Study of Ion Transport in  $Li_2ZrO_3$  Solid Electrolytes with Different Lithium Isotope Ratios. *Crystallogr. Rep.* **2004**, *49*, 676–679. [[CrossRef](#)]
14. Wyers, G.P.; Cordfunke, E.H.P. Phase relations in the system  $Li_2O-ZrO_2$ . *J. Nucl. Mater.* **1989**, *168*, 24–30. [[CrossRef](#)]
15. Shishkin, A.V.; Shishkin, V.Y.; Nikolaev, A.Y.; Pankratov, A.A.; Suzdaltsev, A.V.; Zaikov, Y.P. Reduction of  $ZrO_2$  in  $LiCl-Li_2O$  Melt during Electrolysis. *J. Electrochem. Soc.* **2022**, *169*, 116506. [[CrossRef](#)]
16. Choi, E.-Y.; Meon, M.K.; Kim, S.-W.; Paek, S. Dilution of  $Li-Li_2O$  in a metallic fuel produced through oxide reduction using  $ZrO_2$ -assisted rinsing in molten  $LiCl$ . *J. Nucl. Mater.* **2020**, *533*, 152107. [[CrossRef](#)]
17. Nikolaev, A.; Suzdaltsev, A.; Pavlenko, O.; Zaikov, Y.; Kurennykh, T.; Vykhodets, V. Reduction of  $ZrO_2$  during SNF Pyrochemical Reprocessing. *J. Electrochem. Soc.* **2021**, *168*, 036506. [[CrossRef](#)]
18. Chen, Q.-Y.; Shih, K.-M.; Meng, C.-M.; Liao, C.-Z.; Wang, L.-L.; Xie, H.; Lv, H.-Y.; Wu, T.; Ji, S.-Y.; Huang, Y.-Z. Ab initio density functional theory study of uranium solubility in  $Gd_2Zr_2O_7$  pyrochlores. *Chin. Phys. C* **2015**, 1–20. [[CrossRef](#)]
19. Shu, X.; Qing, Q.; Li, B.; Yang, Y.; Li, L.; Zhang, H.; Shao, D.; Lu, X. Rapid immobilization of complex simulated radionuclides by as-prepared  $Gd_2Zr_2O_7$  ceramics without structural design. *J. Nucl. Mater.* **2019**, *526*, 151782. [[CrossRef](#)]
20. Lang, M.; Zhang, F.; Zhang, J.; Wang, J.; Lian, J.; Weber, W.J.; Schuster, B.; Trautmann, C.; Neumann, R.; Ewing, R.C. Review of  $A_2B_2O_7$  pyrochlore response to irradiation and pressure. *Nucl. Instrum. Methods Phys. Res. B Beam Interact. Mater. At.* **2010**, *268*, 2951–2959. [[CrossRef](#)]
21. Wang, J.; Wang, J.; Zhang, Y.; Li, Y.; Teng, Y.; Wang, Z.; Tan, H. Flux synthesis and chemical stability of Nd and Ce co-doped  $(Gd_{1-x}Nd_x)_2(Zr_{1-x}Ce_x)_2O_7$  ( $0 \leq x \leq 1$ ) pyrochlore ceramics for nuclear waste forms. *Ceram. Int.* **2017**, *43*, 17064–17070. [[CrossRef](#)]
22. Chung, C.K.; Shamblin, J.; O'Quinn, E.C.; Shelyug, A.; Gussev, I.; Lang, M.; Navrotsky, A. Thermodynamic and structural evolution of  $Dy_2Ti_2O_7$  pyrochlore after swift heavy ion irradiation. *Acta Mater.* **2018**, *145*, 227–234. [[CrossRef](#)]
23. Jitta, R.R.; Gundeboina, R.; Veldurthi, N.K.; Guje, R.; Muga, V. Defect pyrochlore oxides: As photocatalyst materials for environmental and energy applications—A review. *J. Chem. Technol. Biotechnol.* **2015**, *90*, 1937–1948. [[CrossRef](#)]
24. Zinatloo-Ajabshir, S.; Salavati-Niasari, M.; Zinatloo-Ajabshir, Z.  $Nd_2Zr_2O_7-Nd_2O_3$  nanocomposites: New facile synthesis, characterization and investigation of photocatalytic behavior. *Mater. Lett.* **2016**, *180*, 27–30. [[CrossRef](#)]
25. Radhakrishnan, A.N.; Rao, P.P.; Mahesh, S.K.; Vaisakhan Thamp, D.S.; Koshy, P. Role of bond strength on the lattice thermal expansion and oxide ion conductivity in quaternary pyrochlore solid solutions. *Inorg. Chem.* **2012**, *51*, 2409–2419. [[CrossRef](#)] [[PubMed](#)]
26. Shlyakhtina, A.; Shcherbakova, L.G. New solid electrolytes of the pyrochlore family. *Russ. J. Electrochem.* **2012**, *48*, 1–25. [[CrossRef](#)]

27. Pavlenko, O.B.; Anokhina, I.A.; Dedyukhin, A.E.; Voronin, V.I.; Nikolaev, A.Y.; Mazannikov, M.V.; Nikitina, E.V.; Karfidov, E.A.; Kholkina, A.S.; Zaikov, Y.P. Interaction between gadolinium zirconate and LiCl–Li<sub>2</sub>O melt. *Ceram. Int.* **2021**, *47*, 20151–20160. [[CrossRef](#)]
28. Zhong, F.; Zhao, J.; Shi, L.; Xiao, Y.; Cai, G.; Zheng, Y.; Long, J. Alkaline-Earth Metals-Doped Pyrochlore Gd<sub>2</sub>Zr<sub>2</sub>O<sub>7</sub> as Oxygen Conductors for Improved NO<sub>2</sub> Sensing Performance. *Sci. Rep.* **2017**, *7*, 4684. [[CrossRef](#)]
29. Anokhina, I.A.; Animitsa, I.E.; Buzina, A.F.; Nokhrin, S.S.; Zaikov, Y.P.; Voronin, V.I.; Vykhodets, V.B.; Kurennykh, T.E.; Kazakova, V.N. Electrical properties of Li<sup>+</sup>-substituted solid solutions based on Gd<sub>2</sub>Zr<sub>2</sub>O<sub>7</sub>. *Russ. J. Phys. Chem. A* **2021**, *95*, 2426–2431. [[CrossRef](#)]
30. Anokhina, I.A.; Animitsa, I.E.; Voronin, V.I.; Vykhodets, V.B.; Kurennykh, T.E.; Molchanova, N.G.; Vylkov, A.I.; Dedyukhin, A.E.; Zaikov, Y.P. The structure and electrical properties of lithium doped pyrochlore Gd<sub>2</sub>Zr<sub>2</sub>O<sub>7</sub>. *Ceram. Int.* **2021**, *47*, 1949–1961. [[CrossRef](#)]
31. Anokhina, I.; Pavlenko, O.; Proskurnina, N.; Dedyukhin, A.; Animitsa, I. The Gd<sub>2-x</sub>Mg<sub>x</sub>Zr<sub>2</sub>O<sub>7-x/2</sub> solid solution: Ionic conductivity and chemical stability in the melt of LiCl–Li<sub>2</sub>O. *Materials* **2022**, *15*, 4079. [[CrossRef](#)] [[PubMed](#)]
32. Golosov, O.A.; Khvostov, S.S.; Glushkova, N.V.; Evseev, M.V.; Staritsyn, S.V.; Zaikov, Y.P.; Kovrov, V.A.; Nikitina, E.V.; Kholkina, A.S.; Kazakovtseva, N.A.; et al. Corrosive and mechanical resistance of MgO ceramics under metallizing and mild chlorination of spent nuclear fuel in molten salts. *Ceram. Int.* **2021**, *47*, 3306–3311. [[CrossRef](#)]
33. Shannon, R.D. Revised effective ionic radii and systematic studies of interatomic distances in halides and chalcogenides. *Acta Cryst.* **1976**, *A32*, 751–767. [[CrossRef](#)]
34. Qu, Z.; Wan, C.; Pan, W. Thermal expansion and defect chemistry of MgO-doped Sm<sub>2</sub>Zr<sub>2</sub>O<sub>7</sub>. *Chem. Mater.* **2007**, *19*, 4913–4918. [[CrossRef](#)]
35. Liu, Z.-G.; Ouyang, J.-H.; Sun, K.-N.; Zhou, Y. Influence of magnesia doping on structure and electrical conductivity of pyro-chlore type GdSmZr<sub>2</sub>O<sub>7</sub>. *Adv. Appl. Ceram.* **2012**, *111*, 214–219. [[CrossRef](#)]
36. Shlyakhtina, A.V.; Abrantes, J.C.C.; Gomes, E.; Lyskov, N.V.; Konysheva, E.Y.; Kharitonova, E.P.; Karyagina, O.K.; Kolbanev, I.V.; Shcherbakova, L.G. Evolution of oxygen-ion and proton conductivity in Ca doped Ln<sub>2</sub>Zr<sub>2</sub>O<sub>7</sub> (Ln = Sm, Gd) zirconates, located near pyrochlore-fluorite phase boundary. *Materials* **2019**, *12*, 2452. [[CrossRef](#)] [[PubMed](#)]
37. Jiang, L.; Wang, C.; Wang, J.; Liu, F.; You, R.; Lv, S.; Zeng, G.; Yang, Z.; He, J.; Liu, A.; et al. Pyrochlore Ca-doped Gd<sub>2</sub>Zr<sub>2</sub>O<sub>7</sub> solid state electrolyte type sensor coupled with ZnO sensing electrode for sensitive detection of HCHO. *Sens. Actuators B Chem.* **2020**, *309*, 127768. [[CrossRef](#)]
38. Cho, S.H.; Park, S.B.; Lee, J.H.; Hur, J.M.; Lee, H.S. Hot corrosion behavior of ZrO<sub>2</sub>–MgO coatings in LiCl–Li<sub>2</sub>O molten salt. *Mater. Chem. Phys.* **2012**, *131*, 743–751. [[CrossRef](#)]
39. Valtseva, A.I.; Pershin, P.S.; Suzdaltsev, A.V.; Zaikov, Y.P. Research of oxygen-conducting ceramic materials for lithium chloride melt in reactors for pyrochemical processing of spent nuclear fuel. *J. Phys. Conf. Ser.* **2020**, *1683*, 032029. [[CrossRef](#)]

**Disclaimer/Publisher’s Note:** The statements, opinions and data contained in all publications are solely those of the individual author(s) and contributor(s) and not of MDPI and/or the editor(s). MDPI and/or the editor(s) disclaim responsibility for any injury to people or property resulting from any ideas, methods, instructions or products referred to in the content.